H. Hasegawa[1], R. E. Denton[2], T. K. M. Nakamura[3,4], K. J. Genestreti[5], T. D. Phan[6], R. Nakamura[3], K.-J. Hwang[7], N. Ahmadi[8], Q. Q. Shi[9], M. Hesse[10], J. L. Burch[7], J. M. Webster[7], R. B. Torbert[4,11], B. L. Giles[12], D. J. Gershman[12], C. T. Russell[13], R. J. Strangeway[13], H. Y. Wei[13], P.-A. Lindqvist[14], Y. V. Khotyaintsev[15], R. E. Ergun[16], and Y. Saito[1]

[1]Institute of Space and Astronautical Science, Japan Aerospace Exploration Agency, Sagamihara, Japan.

[2]Department of Physics and Astronomy, Dartmouth College, Hanover, NH, USA.

[3]Space Research Institute, Austrian Academy of Sciences, Graz, Austria.

[4]Institute of Physics, University of Graz, Graz, Austria.

[5]Southwest Research Institute, Durham, NH, USA.

[6]Space Sciences Laboratory, University of California, Berkeley, CA, USA.

[7]Southwest Research Institute, San Antonio, TX, USA.

[8]Laboratory for Atmospheric and Space Physics, University of Colorado, Boulder, CO, USA.

[9]Shandong Provincial Key Laboratory of Optical Astronomy and Solar-Terrestrial Environment, Institute of Space Sciences, Shandong University, Weihai, China.

[10]Space Plasma Physics Group, University of Bergen, Bergen, Norway.

[11]Physics Department, University of New Hampshire, Durham, NH, USA.

[12]NASA Goddard Space Flight Center, Greenbelt, MD, USA.

[13]Department of Earth, Planetary, and Space Sciences, University of California, Los Angeles, CA, USA.

[14]Royal Institute of Technology, Stockholm, Sweden.

[15]Swedish Institute of Space Physics, Uppsala, Sweden.

[16]Department of Astrophysical and Planetary Sciences, University of Colorado, Boulder, CO, USA.

Corresponding author: Hiroshi Hasegawa (`hase@stp.isas.jaxa.jp`)

Key Points:

- Multispacecraft observations consistent with magnetic field annihilation in an electron diffusion region (EDR) of magnetotail reconnection
- Magnetic field reconstruction suggests that an electron-scale magnetic island was embedded in the EDR with elongated shape

- Theoretical analysis shows that fast collisionless magnetic diffusion can occur in the elongated part of EDR with nongyrotropic electrons

Abstract

We present observations in Earth's magnetotail by the Magnetospheric Multiscale spacecraft that are consistent with magnetic field annihilation, rather than magnetic topology change, causing fast magnetic-to-electron energy conversion in an electron-scale current sheet. Multi-spacecraft analysis for the magnetic field reconstruction shows that an electron-scale magnetic island was embedded in the observed electron diffusion region (EDR), suggesting an elongated shape of the EDR. Evidence for the annihilation was revealed in the form of the island growing at a rate much lower than expected for the standard collisionless reconnection, which indicates that magnetic flux injected into the EDR was not ejected from the X-point or accumulated in the island, but was dissipated in the EDR. This energy conversion process is in contrast to that in the standard EDR of a reconnecting current sheet where the energy of antiparallel magnetic fields is mostly converted to electron bulk-flow energy. Fully kinetic simulation also demonstrates that an elongated EDR is subject to the formation of electron-scale magnetic islands in which fast but transient annihilation can occur. Consistent with the observations and simulation, theoretical analysis shows that fast magnetic diffusion can occur in an elongated EDR in the presence of nongyrotropic electron effects. We suggest that the annihilation in elongated EDRs may contribute to the dissipation of magnetic energy in a turbulent collisionless plasma.

**Plain Language Summary**

Magnetic reconnection in electric current sheets is the key to fast release of magnetic energy in many space and astrophysical plasma systems, such as during magnetospheric substorms and solar flares. Establishing the mechanism by which magnetic energy is converted to particle energy in the reconnection process is the key to understanding the large-scale impacts of reconnection, including energy partition and particle acceleration. It is generally believed that an electron-scale diffusion region (EDR), where a magnetic-to-electron energy conversion occurs, has an X-type magnetic field geometry around which the energy of antiparallel magnetic fields injected into the EDR is mostly converted to the bulk-flow energy of electrons by magnetic tension of reconnected field lines. Contrary to this standard X-type magnetic field geometry of reconnection, we report observations in Earth's magnetotail by NASA's Magnetospheric Multiscale spacecraft showing that the EDR can be highly elongated. The important and surprising consequence of the observed elongated shape of the EDR is that the fast energy conversion in the EDR can be caused mostly by magnetic field annihilation, rather than magnetic topology change. The fast collisionless annihilation that we discovered is fundamentally different from the classical magnetic field annihilation due to collisional and wave-induced resistivity.

## 1 Introduction

Magnetic reconnection in Earth's magnetotail is fast, with an inflowing plasma speed of ~0.1 times the Alfvén speed in the inflow region, and has large-scale impacts, for example, explosive release of magnetic energy during magnetospheric substorms (Angelopoulos et al., 2008; Nagai et al., 2011). Magnetotail reconnection occurs under such simple boundary conditions that on the two sides of the current sheet the magnetic field is approximately oppositely-directed with a comparable intensity, and plasmas have similar densities and temperatures. Such nearly antiparallel and symmetric reconnection is ideal for studying intrinsic properties of magnetic reconnection in the collisionless regime.

In the standard model of reconnection, the electron diffusion region (EDR), where the 'frozen-in condition' is violated for both ions and electrons, is localized with an X-type field geometry where a magnetic-to-electron energy conversion occurs by changing the magnetic field topology (Torbert et al., 2018). It is generally accepted that in such EDRs most of the energy of antiparallel magnetic fields injected by the inflow is converted to bulk-flow energy of electrons ejected into the regions downstream of the EDR (Shay et al., 2007), called the exhausts, by magnetic tension (Lorentz force) of reconnected field lines. Numerical simulations suggest that the EDR may be elongated in the outflow direction to form a planar geometry (Daughton et al., 2006; Fujimoto, 2006), and an elongated EDR is subject to the formation of electron-scale magnetic islands, likely through the electron tearing instability (Nakamura et al., 2021). The conventional wisdom is that the elongation of the EDR results in a substantial reduction of the reconnection rate (Daughton et al., 2006; Fujimoto, 2006). However, a fully kinetic simulation by Nakamura et al. (2021) shows that the reconnection rate defined as the rate of in-plane magnetic flux injection to the dominant X-point can remain high (~0.1 in dimensionless units) even during the phase when the EDR is elongated (see their Figure 2d), and suggests that fast energy conversion can be sustained by magnetic field annihilation, rather than field topology change, for about one ion cyclotron period.

Figure 1 shows time evolution of the in-plane magnetic field and energy conversion rate in and around the EDR for time $t = 55.4\Omega_i^{-1}$ to $56.2\Omega_i^{-1}$, seen in the two-dimensional (2-D) simulation reported by Nakamura et al. (2021). Here, $\Omega_i$ is ion gyrofrequency, and the ion to electron mass ratio is 400 (see Text S1 for details of the simulation settings). The energy conversion rate $\mathbf{j} \bullet (\mathbf{E}+\mathbf{v}_e \times \mathbf{B})$ is significantly positive in the electron-scale current sheet throughout the interval, indicating that significant magnetic-to-particle energy conversion continuously occurs there. This is consistent with the fact that the minimum of partial magnetic vector potential (flux function) $A_M$, corresponding to $A_M$ at the most dominant X-point, continuously decreases with time (Figure 1f), because $\frac{\partial A_M}{\partial t} = -E_M$ (see Figure 2d of Nakamura et al. (2021) for the actual time evolution of $E_M$). In 2-D, the motion of a specific magnetic field line can be tracked by tracing the location of equal vector potential values $A_M$ in time. In the absence of magnetic field annihilation, $A_M$ at the O-point, which corresponds to the center of magnetic islands and can be identified as a local $A_M$

maximum in Figure 1f, should be constant in time. This is because in such cases the in-plane magnetic flux injected to the X-point would be reconnected, ejected toward the exhausts, and accumulated in the island. This is roughly the case when the island size is near or larger than the ion inertial length ($d_{i0} = 20d_{e0}$), as seen in Figure 1d,e for $t = 56.0\Omega_i^{-1}$ to $56.2\Omega_i^{-1}$ when $\mathbf{j} \bullet (\mathbf{E}+\mathbf{v}_e \times \mathbf{B})$ is nearly zero around the O-point.

On the other hand, $A_M$ at the O-point continuously decreases from $t = 55.4\Omega_i^{-1}$ to $56.0\Omega_i^{-1}$ when $\mathbf{j} \bullet (\mathbf{E}+\mathbf{v}_e \times \mathbf{B})$ is significantly positive not only at the X-point but also around the O-point. Note that an electron-scale magnetic island is formed already at $t = 55.4\Omega_i^{-1}$ when the EDR is elongated (very small local maximum in red curve of Figure 1f at $\frac{L}{d_{e0}} \sim 1019$; see also Figure 3f of Nakamura et al. (2021)). The continuous $A_M$ decrease at the O-point is evidence from the simulation that the annihilation of in-plane magnetic field is occurring in the electron-scale island. At present, it remains unclear whether the annihilation of $B_L$ around the X-point or that of $B_N$ around the O-point is dominant. Thus, the annihilation in the present study may be defined as non- or weak-ejection of in-plane magnetic flux out of the X-point due to $B_L$ diffusion, or diffusion of the reconnected field component $B_N$ at the O-point, under the presence of significant $E_M$. It is probable, however, that the electron-scale annihilation is mostly due to that of $B_L$ because the diffusion process is more efficient in regions where the gradient of the corresponding quantity (in-plane magnetic field in the present case) is larger (see also section 4).

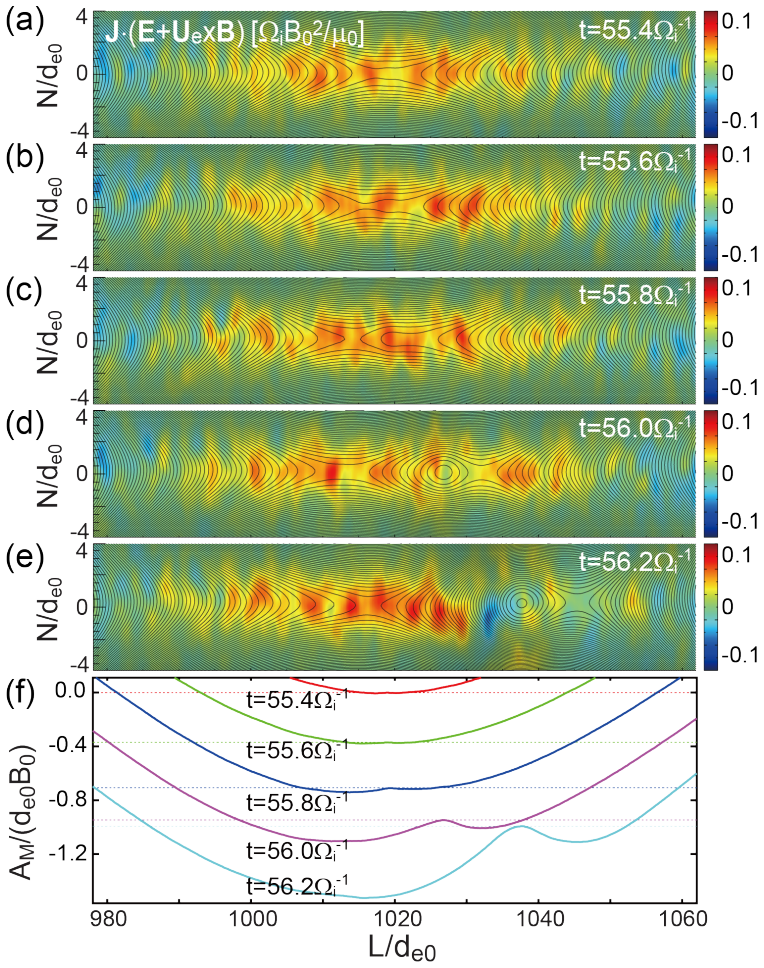


**Figure 1**. (a-e) Time evolution of an electron diffusion region (EDR) from a fully kinetic simulation of turbulent magnetic reconnection (Nakamura et al., 2021), showing EDR elongation and island growth on the scale of electron inertial length $d_{e0}$. In-plane magnetic field lines are shown by black curves and energy conversion rate $\mathbf{j} \bullet (\mathbf{E} + \mathbf{v}_e \times \mathbf{B})$ (Zenitani et al., 2011) in color, where $\mathbf{E}$ and $\mathbf{B}$ are the electric and magnetic fields, respectively, $\mathbf{j}$ current density, and $\mathbf{v}_e$ electron flow velocity. (f) Simulated vector potential (flux function) $A_M$ along $N = 0$ for selected times. It shows that $A_M$ at the O-point (local $A_M$ maximum, marked by the horizontal dashed lines) continuously decreases from $t = 55.4\Omega_i^{-1}$ to $56.0\Omega_i^{-1}$ at a rate comparable to that at the primary X-point ($A_M$ minimum), demonstrating that magnetic field annihilation occurs in and around the island.

Since the collisionless magnetic field annihilation on the electron scale has only recently been identified in simulation (Nakamura et al., 2021), it remains un-

known if such a process can actually occur in spatially extended EDRs with negligibly small reconnected field components in space. This is also because unambiguous identification of EDR structures in space requires high-spatiotemporal-resolution plasma measurements, and there has been no data analysis method to distinguish whether the magnetic field injected into the EDR is reconnected or annihilated.

In this paper, we present in-depth analysis of the fortuitous multi-spacecraft observations by the Magnetospheric Multiscale (MMS) mission (Burch et al., 2016) of a magnetotail EDR and electron-scale magnetic island on 10 August 2017 (Zhou et al., 2019), in which the magnetic-to-particle energy conversion rate was consistent with fast reconnection. Contrary to the standard model of reconnection with an X-type field geometry at the EDR, however, our analysis suggests that the EDR was elongated in the outflow direction and the fast energy conversion observed in the EDR was supported by magnetic field annihilation, rather than magnetic topology change. Consistent with this interpretation, our theoretical analysis shows that fast magnetic diffusion can occur in an elongated EDR in the presence of nongyrotropic electron effects, and may lead to magnetic field annihilation within electron-scale islands.

## 2 Overview of the Observations

For this study, MMS burst-mode data from the following instrument suites were used: FIELDS (Torbert et al., 2016), including the electric field instruments (Lindqvist et al., 2016; Ergun et al., 2016) and magnetometers (Russell et al., 2016), and Fast Plasma Investigation (FPI) for electron and ion plasma distributions and moments (Pollock et al., 2016).

In Figures 2a-2d, we show the context of the reconnecting current sheet observed by the MMS2 spacecraft on 10 August 2017 at 12:17:40–12:19:40 UT, when MMS was fully embedded in the hot magnetotail plasma sheet (Zhou et al., 2019) at $(-15.2,\ \ 4.6,\ 3.1)\ R_E$ in GSM coordinates. The current sheet at 12:18:30 UT is characterized by a reversal from anti-sunward to sunward ion flows (negative to positive $v_{ix}$ change in Figure 2b), crossing from its southern to northern side (negative to positive $B_x$ change in Figure 2a). The ion flow speeds around the start and end of the interval are comparable to the ion Alfvén speed $V_{\rm iA} = \frac{B}{(\mu_0\rho)^{\frac{1}{2}}} \approx 850$ km s$^{-1}$ based on the magnetic field intensity $B \approx 15$ nT and proton number density of 0.15 cm$^{-3}$, where $\mu_0$ is the vacuum permeability and $\rho$ is plasma mass density. A fast dawnward electron flow ($v_{ey} \approx -10$ Mm $s^{-1}$ in Figure 2c) and a relatively slow duskward ion flow with no enhancement at the current sheet show that its electric current was supported by electrons. These features indicate that MMS crossed an electron-scale current sheet (ECS) embedded inside a region of large-scale reconnection when traversing from its anti-sunward exhaust to sunward exhaust. Earlier studies of this current sheet (Zhou et al., 2019; Li et al., 2019) reported established signatures of EDRs (Burch et al., 2016; Torbert et al., 2018), including oppositely-directed electron jets with a speed exceeding $V_{\rm iA}$ (Figure 2c), crescent-shaped electron velocity

distributions, and magnetic-to-particle energy conversion.

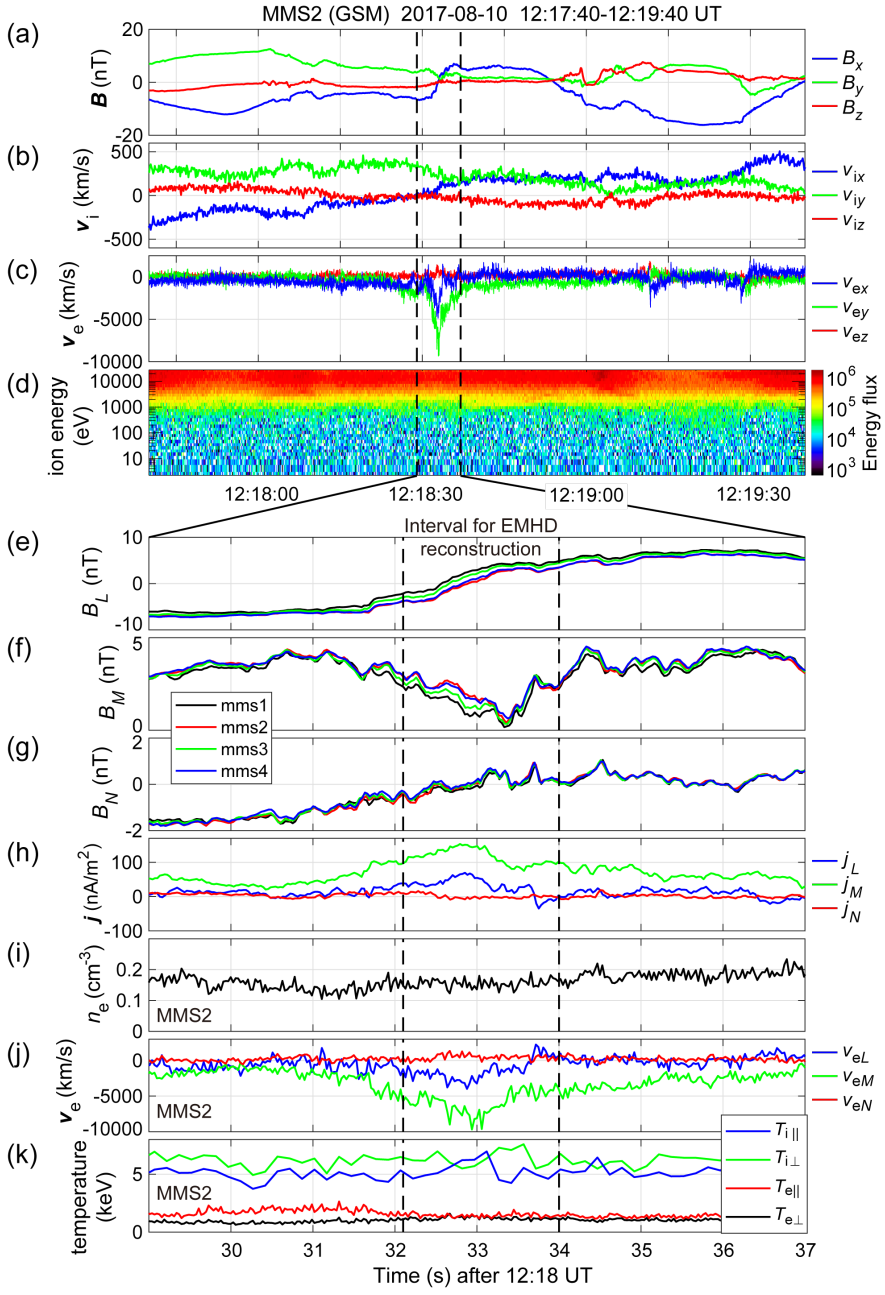


**Figure 2**. Overview of MMS observations of an electron-scale current sheet with both ion and electron reconnection jet signatures. (a-d) GSM components of the magnetic field (a; $B_x$, $B_y$ and $B_z$), ion velocity (b; $v_{ix}$, $v_{iy}$ and $v_{iz}$),

electron velocity (c; $v_{ex}$, $v_{ey}$ and $v_{ez}$) and ion energy-time spectrogram of omni-directional differential energy flux (d; color scale, in units of keV $s^{-1}$ $cm^{-2}$ $sr^{-1}$ $keV^{-1}$) seen by MMS2. (e-h) Components in a common current-sheet (LMN) coordinate system of the magnetic field (e-g; $B_L$, $B_M$ and $B_N$) from all four spacecraft (black, MMS1; red, MMS2; green, MMS3; blue, MMS4) and current density $\mathbf{j}=\frac{(\nabla\times\mathbf{B})}{\mu_0}$ (Dunlop et al., 2002) (h; $j_L$, $j_M$ and $j_N$). (i-k) MMS2 measurements of the electron density (i; $n_e$), electron velocity in LMN coordinates (j; $v_{eL}$, $v_{eM}$ and $v_{eN}$), and ion and electron temperatures (k; $T_i$ and $T_e$) in the directions parallel ($\parallel$) and perpendicular ($\perp$) to the local magnetic field. GSM components of the LMN axes are: $\mathbf{L} = (0.955,\ -0.298,\ -0.021)$, $\mathbf{M} = (0.296,\ 0.953,\ -0.059)$, and $\mathbf{N} = (0.038,\ 0.050,\ 0.998)$ (section 3.2).

## 3 Reconstruction of the Electron-scale Current Sheet

We investigate the ECS structure in detail by use of two sophisticated data analysis techniques that can reconstruct multi-dimensional magnetic field structures in regions around the spacecraft from in situ measurements of the magnetic field and plasma bulk parameters. One is a single-spacecraft method based on electron-magnetohydrodynamics (EMHD) equations that can recover quasi-steady, two-dimensional (2-D) magnetic, electrostatic, and electron velocity fields around the path of the observing spacecraft, hereafter called EMHD reconstruction (Sonnerup et al., 2016; Hasegawa et al., 2021; Text S2). The other is a multi-spacecraft method based on polynomial (second-order Taylor) expansion of the magnetic field that can recover three-dimensional (3-D) magnetic field using instantaneous measurements by the four spacecraft of the magnetic field and particle current density, called polynomial reconstruction (Denton et al., 2020; Text S3).

### 3.1 Dimensionality of the Structure

To analyze the dimensionality of the ECS, the Maximum Directional Derivative (MDD) method (Shi et al., 2019) was applied to four-spacecraft measurements of the magnetic field for an interval 12:18:29–12:18:37 UT surrounding the reconstruction interval (Figure 3). Figures 3e,f show that the maximum eigenvalue $\lambda_{max}$ is much larger than the other two eigenvalues and the first dimension number index $D_1$ (Rezeau et al., 2018) is much larger than the other two indices, suggesting that the magnetic structure of the ECS was locally nearly 1-D during the reconstruction interval. Figure 3g shows that $\mathbf{k}_{\max}$, which can be taken as the ECS normal direction, was stably northward throughout the reconstruction interval. These results indicate that the ECS was approximately planar with no significant undulation on the scale of the spacecraft separation ~18 km which was comparable to the electron inertial length ($d_e \sim 14$ km). The fact that $\lambda_{mid}$ is somewhat larger than $\lambda_{min}$ (Figure 3e) suggests that although the ECS was nearly 1-D, there were some 2-D structures that may be recovered by the EMHD reconstruction.

### 3.2 Data in the LMN Coordinate System

Figures 2e-2k show the magnetic field and plasma data from MMS, used as input for the two reconstruction techniques, in a current-sheet ('LMN') coordinate system: the current-sheet normal points along $\mathbf{N}$ (roughly northward in the magnetotail), the reconnecting antiparallel magnetic field component is along $\mathbf{L}$ (roughly sunward), and $\mathbf{M} = \mathbf{N} \times \mathbf{L}$ is along the 'X-line' direction (roughly duskward). The final LMN coordinate system used in this study (Figure 2 caption) was determined through optimization of the EMHD reconstruction results, as detailed in section 3.4. A preliminary LMN coordinate system used as trial LMN axes in the reconstruction was determined by a hybrid method (Denton et al., 2018), which combines the Maximum Variance Analysis (MVA) of the magnetic field (Sonnerup & Scheible, 1998) and Maximum Directional Derivative (MDD) method (Shi et al., 2019) applied to four-spacecraft measurements of the magnetic field at 12:18:31–12:18:36 UT. The resulting LMN axes are: $\mathbf{L}_p = (0.992,\ -0.127,\ -0.022)_{\mathrm{GSM}}$, $\mathbf{M}_p = (0.127,\ 0.992,\ -0.003)_{\mathrm{GSM}}$, and $\mathbf{N}_p = (0.022,\ -0.000,\ 1.000)_{\mathrm{GSM}}$, which are not very different from the final axes.

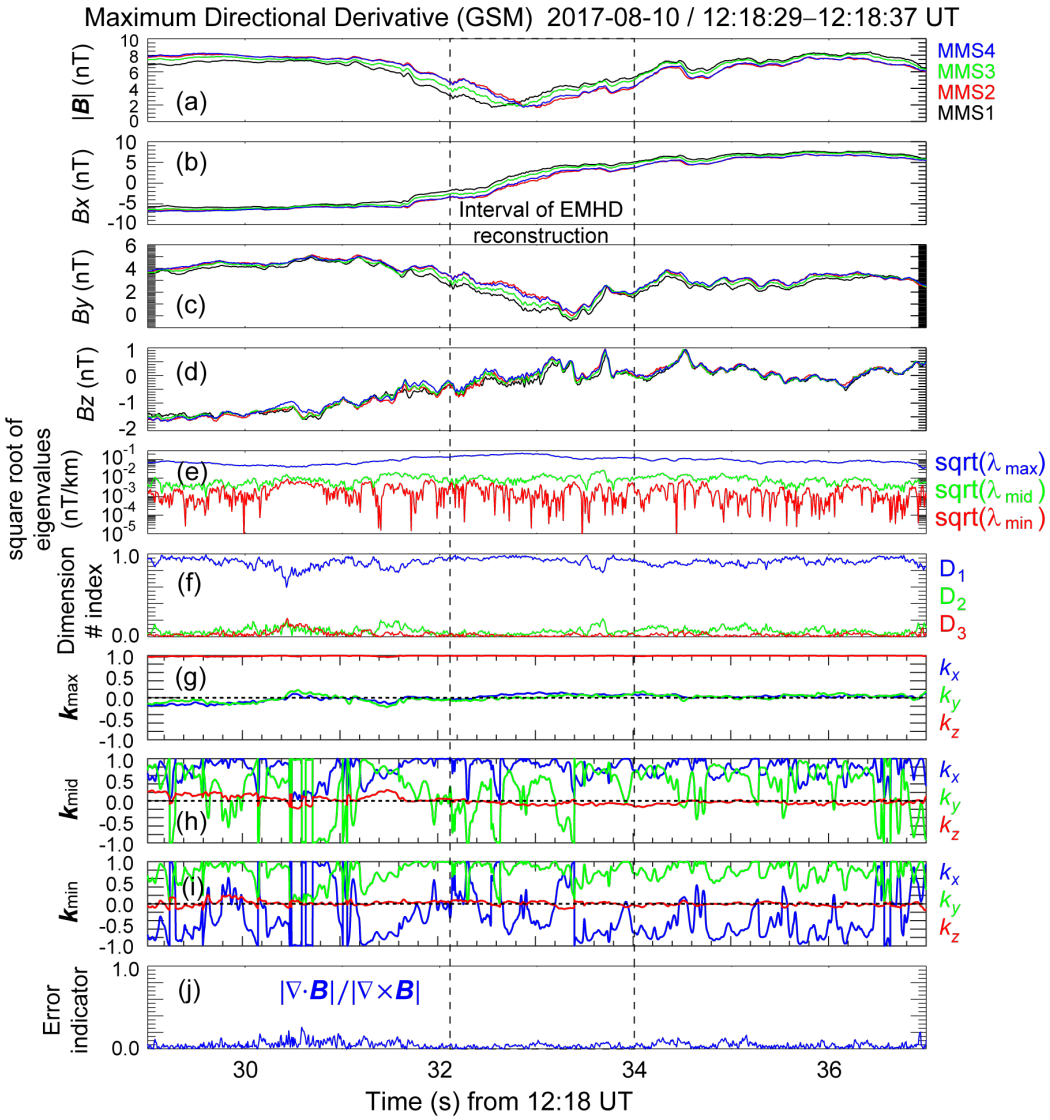


**Figure 3**. Results from the MDD method (Shi et al., 2019) applied to an interval 12:18:29–12:18:37 UT. (a-d) GSM components of the magnetic field measured by the four MMS spacecraft (a; $|\mathbf{B}|$, b; $B_x$, c; $B_y$, d; $B_z$). (e) Square roots of the maximum, intermediate, and minimum eigenvalues ($\lambda_{\max}$, $\lambda_{\mathrm{mid}}$, $\lambda_{\min}$) of the $3 \times 3$ MDD matrix (Shi et al., 2019). (f) Dimension number indices (Rezeau et al., 2018), defined as $D_1 = \frac{(\lambda_{\max}-\lambda_{\mathrm{mid}})}{\lambda_{\max}}$, $D_2 = \frac{(\lambda_{\mathrm{mid}}-\lambda_{\min})}{\lambda_{\max}}$, and $D_3 = \frac{\lambda_{\min}}{\lambda_{\max}}$, that can be used as measures of the dimensionality of the structure encountered by the spacecraft. (g-i) Eigenvectors corresponding to the three eigenvalues (g: $\mathbf{k}_{\max}$; h: $\mathbf{k}_{\mathrm{mid}}$; i: $\mathbf{k}_{\min}$). (j) $\frac{|\nabla \bullet \mathbf{B}|}{|\nabla \times \mathbf{B}|}$ as an error proxy.

A weak guide field (~2 nT) (Zhou et al., 2019), the component ($B_M$) along the X-line of the magnetic field external to the entire larger-scale current sheet, or, in this case, at the center of the ECS (Figure 2f), confirms that reconnection occurred under nearly antiparallel magnetic field conditions. Negative to positive variation of $B_N$ (Figure 2g) is consistent with MMS moving from the anti-sunward to sunward side of the reconnection site; the X-line was moving anti-sunward (section 3.3). The assumptions of constant density and constant and isotropic electron temperature made in the EMHD reconstruction are approximately satisfied for an intense current density interval at 12:18:32.1–12:18:34.0 UT (Figures 2i,k), to which the method is applied.

### 3.3 Frame Velocity

The EMHD reconstruction is performed in a frame of reference comoving with the structure. It was estimated by a multi-spacecraft data-analysis technique known as the spatiotemporal difference (STD) method (Shi et al., 2019), applied to smoothed magnetic field data from the four spacecraft at 12:18:32.0–12:18:33.3 UT. The velocity component from the STD method along the minimum magnetic-gradient direction $\mathbf{k}_{\rm min}$, which is often along $\mathbf{M}$ (Figure 3i), is usually unreliable (Denton et al., 2016) and was not used. The resulting velocity is $\mathbf{V}_{\rm STD} = -100\mathbf{L}_p - 28\mathbf{N}_p$ km $s^{-1}$, consistent with an anti-sunward moving EDR and south-to-north crossing of the ECS. The normal velocity roughly agrees well with that ($-35$ $km$ $s^{-1}$) estimated by multi-spacecraft timing analysis (Zhou et al., 2019). The $L$-component dominated motion of the structure, combined with the approximately planar geometry of the ECS (Figure 3f), indicates that the ECS was elongated in the outflow direction. The $L$ and $N$ components of the final structure velocity $\mathbf{V}_{\rm str} = (-30,\ 237,\ -40)_{\rm GSM}$ km s$^{-1}$, used in the EMHD reconstruction, are the projections along $\mathbf{L}$ and $\mathbf{N}$ of $\mathbf{V}_{\rm STD}$ and the $M$ component ($V_{str,M}$) is that of the mean ion velocity for the reconstruction interval, so that the electric current is supported mostly by electrons in the structure frame.

### 3.4 EMHD Reconstruction

Figure 4 shows the magnetic field, electron streamlines, and electric field reconstructed for the present ECS from the EMHD reconstruction technique including electron inertia effects but assuming incompressiblity (i.e., constant density) (Hasegawa et al., 2021). The input data were taken during a 1.9 s interval 12:18:32.1–12:18:34.0 UT from MMS3, which was located near the centroid of the MMS tetrahedron in the reconstruction plane. The final LMN axes were optimized by a multi-spacecraft method (Hasegawa et al., 2019), which searches for the invariant-axis ($\hat{\mathbf{z}}_{\rm EMHD}$) orientation that maximizes the correlation coefficient (Figure 4d) between the normalized components of the magnetic field and electron velocity measured by three spacecraft not used as input in the reconstruction and those predicted at points along the paths of the three spacecraft from the reconstructed field maps. The reconstruction axes thus determined are: $\hat{\mathbf{x}}_{\rm EMHD} = (0.927,\ -0.271,\ 0.260)_{\rm GSM}$, $\hat{\mathbf{y}}_{\rm EMHD} = (-0.232,\ 0.131,\ 0.964)_{\rm GSM}$ and $\hat{\mathbf{z}}_{\rm EMHD} = (-0.296,\ -0.953,\ 0.059)_{\rm GSM}$.

The reconstructed streamlines (Figure 4b) clearly show the inflow and outflow patterns as expected for 2-D reconnection but have a complex structure, probably because of the presence of an electron-scale magnetic island (Figure 4a), and time evolution associated with its growth (Figure 5). Note, however, that a quadrupolar pattern of $B_{z,EMHD} = -B_M$ related to the Hall effect (Nagai et al., 2001; Øieroset et al., 2001) is roughly reconstructed. The electron stagnation point appears to be located near the O-point, rather than the X-point. Such a displacement in the outflow direction of the X and stagnation point has been observed for another magnetotail EDR event reported by Torbert et al. (2018) (Hasegawa et al., 2019).

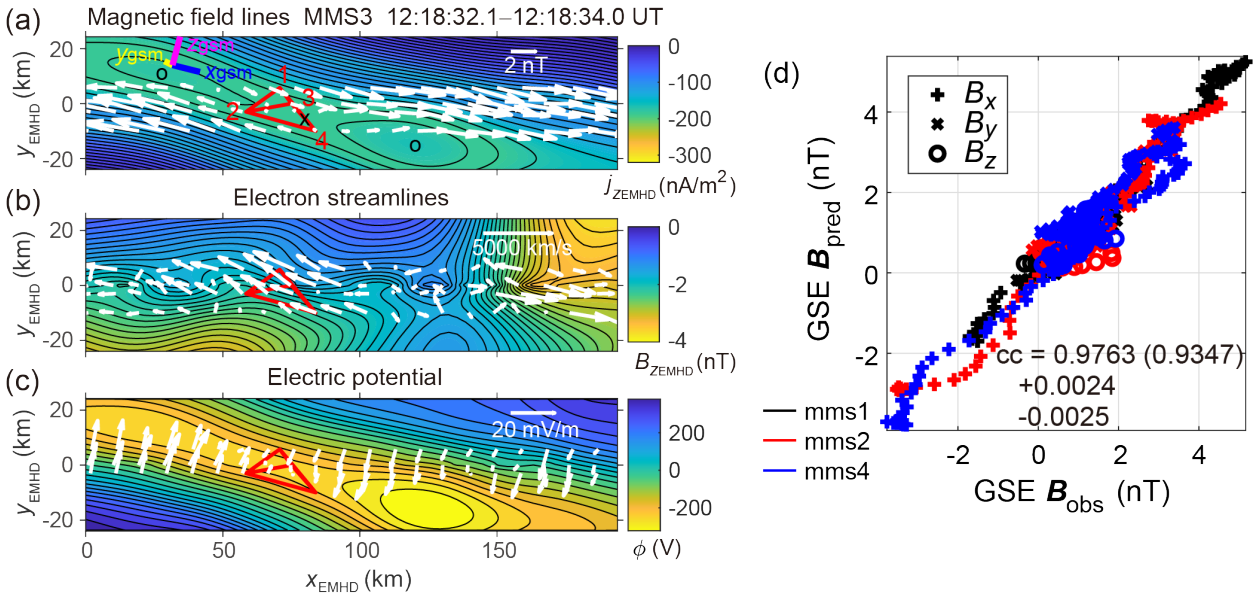


**Figure 4**. 2-D magnetic, electrostatic and electron-velocity fields recovered from the EMHD reconstruction applied to the MMS 3 data at 12:18:32.1–12:18:34.0 UT. (a) Reconstructed in-plane magnetic field-lines with the out-of-plane component ($j_{z,EMHD}$) of the reconstructed current density in color. White arrows show the projections onto the reconstruction plane of the measured magnetic fields along the paths ($y_{\mathrm{EMHD}} = const.$) of the four spacecraft. (b) Reconstructed electron streamlines with the out-of-plane component ($B_{z,EMHD}$) of the reconstructed magnetic field in color. The arrows show the projections of the measured electron velocities transformed into the structure-rest frame. (c) Reconstructed electrostatic potential ($\phi$), along with the projections of the measured electric field ($\mathbf{E}_{\mathrm{str}} = \mathbf{E} + \mathbf{V}_{\mathrm{str}} \times \mathbf{B}$) transformed into the structure-rest frame. (d) Correlation between the components in geocentric solar ecliptic (GSE) coordinates of the measured magnetic field ($B_x$: plus, $B_y$: cross, and $B_z$: circle) and those predicted from the reconstruction along the paths of MMS 1 (black), MMS 2 (red), and MMS 4 (blue) not used as input for the reconstruction. The confidence intervals of the correlation coefficients corresponding to

±1 sigma were estimated by the bootstrap method (Kawano & Higuchi, 1995). The value in the parenthesis is the correlation coefficient between the values measured by MMS3 (used as input for the reconstruction) and those measured during the same interval by the other three spacecraft, with an aim to demonstrate whether the reconstruction provides better prediction along the paths of the other three spacecraft.

Figure 4d shows that the magnetic field is well reconstructed with a very high correlation coefficient, which suggests that the reconstruction coordinate system is well determined. We emphasize that the correlation coefficient between the predicted and measured values is larger than that between the input values measured by MMS3 and the values measured during the same interval by the other three spacecraft but interpolated to the times of the MMS3 measurements (correlation coefficient in the parenthesis in Figure 4d). The spacecraft separation ~18 km was comparable to the island thickness of order $d_e \sim 14$ km. Thus, the high correlation suggests that we may rely on the reconstructed magnetic fields on those spatial scales.

### 3.5 Comparison among the Four Spacecraft and with Polynomial Reconstruction

Figure 5 shows the 2-D representation of the magnetic field reconstructed from the EMHD and polynomial reconstructions (Text S3). Both reconstruction results (Figures 5a-d and 5f-i) clearly show that an electron-scale magnetic island was forming and growing in the ECS with a thickness of about one $d_e$. This is consistent with the MDD result suggesting that the ECS had a planar and elongated configuration (Figure 3), ideal for island generation (Daughton et al., 2006). The island size in the $L$ direction may look shorter than the fastest growing wavelength (of order $10d_e$) of the electron tearing instability (Jain & Sharma, 2015), but note that such small islands have been seen in kinetic simulations (Figure 3 of Nakamura et al., 2021).

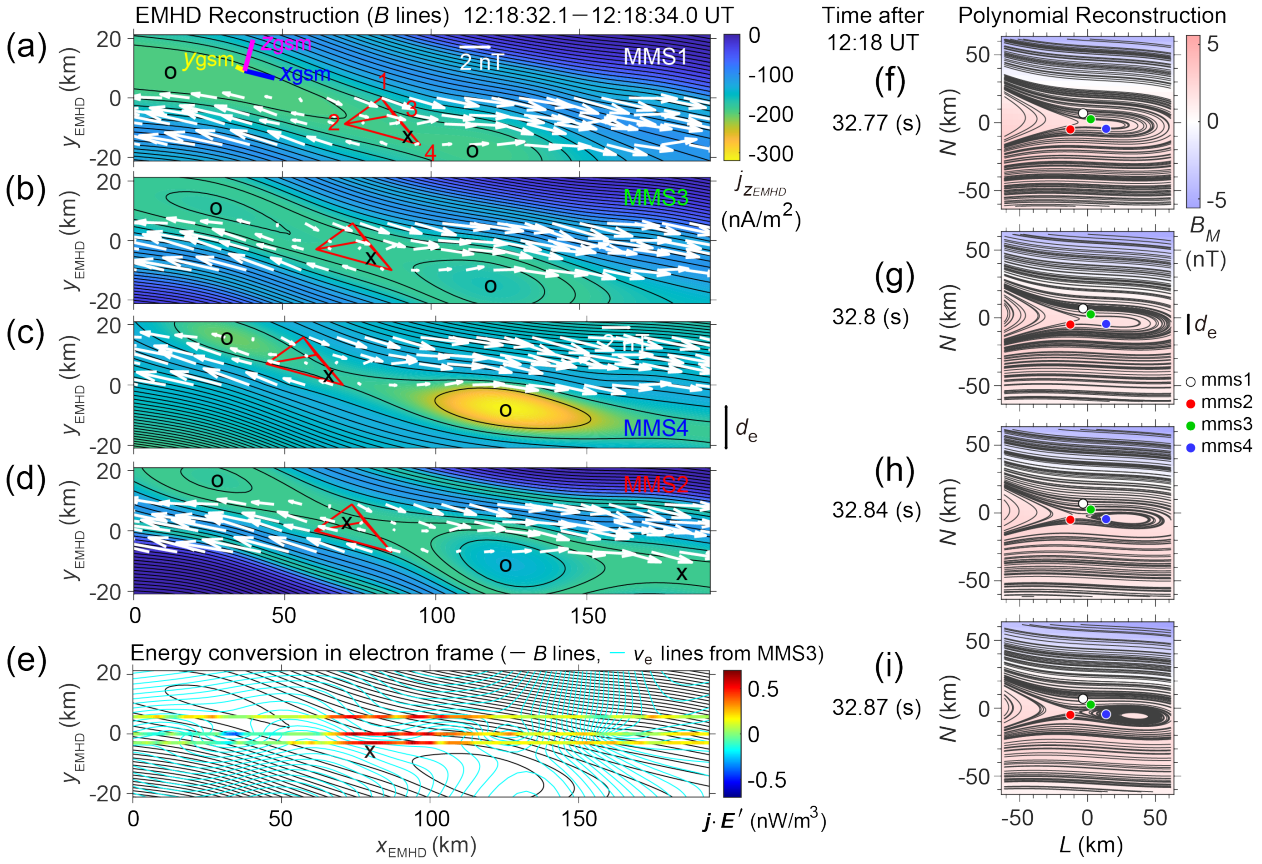


**Figure 5**. Magnetic fields recovered from the EMHD and polynomial reconstruction methods (Texts S2 and S3). (a-d) 2-D magnetic fields from the EMHD reconstruction with electron inertia effects (Hasegawa et al., 2021) using the data taken at 12:18:32.1–12:18:34.0 UT individually for each of the four spacecraft, shown in the order of current sheet crossing (MMS1, a; MMS3, b; MMS4, c; then MMS2, d; as seen in Figure 2e). Black curves show the reconstructed magnetic field-lines, colors the out-of-plane component ($j_{z,EMHD}$) of the reconstructed current density, and white arrows the projections onto the reconstruction ($x_{\mathrm{EMHD}}$–$y_{\mathrm{EMHD}}$) plane of the measured magnetic fields along the paths of the four spacecraft. The bars near the upper-left corner of panel (a) are the projections of the unit GSM axes (blue, $\hat{\mathbf{x}}_{\mathrm{GSM}}$; yellow, $\hat{\mathbf{y}}_{\mathrm{GSM}}$; magenta, $\hat{\mathbf{z}}_{\mathrm{GSM}}$). (e) Magnetic field lines (black curves) and electron streamlines (blue curves) reconstructed from the MMS 3 data, with $\mathbf{j}_p \bullet \mathbf{E}'$ (Zenitani et al., 2011) measured along the paths of MMS 1, MMS 2, and MMS 3 in color. (f-i) Projection onto the $L$–$N$ plane of 3-D magnetic field-lines reconstructed using the polynomial reconstruction (Denton et al., 2020) from instantaneous measurements by the four spacecraft of $\mathbf{B}$ and $\mathbf{j}_p$, with reconstructed $B_M$ in color.

Figures 5a-d show that over a ~0.4 s interval of 12:18:32.6–12:18:33.0 UT, during which the current sheet was crossed in the order of MMS 1, MMS 3, MMS 4, and MMS 2 (Figure 2e), both the length (along **L**) and width (along **N**) of the island grew. An entirely consistent feature is seen in Figures 5f-i. The time scale (~0.4) of the ECS crossing is comparable to the proton cyclotron period, so that the island growth was probably slow on the electron time scale. This feature is further confirmed by slow accumulation of in-plane magnetic flux in the island (Figure 6); the quasi-steady assumption of the EMHD reconstruction is approximately satisfied.

Despite the slow growth of the island, the energy-conversion rate $\mathbf{j} \bullet \mathbf{E}' = \mathbf{j}_p \bullet (\mathbf{E} + \mathbf{v}_e \times \mathbf{B})$ (Zenitani et al., 2011) (Figure 5e), where the particle current density is $\mathbf{j}_p = en_e (\mathbf{v}_i - \mathbf{v}_e)$ with the elementary charge of $e$ and **E** the electric field measured in the spacecraft frame, is strongly positive around an X-point closer to the center of the reconstruction domain. Its magnitude (~0.5 nW $m^{-3}$) is comparable to the value (~0.2 nW $m^{-3}$) expected for fast collisionless reconnection, based on the current density ~150 nA $m^{-2}$ (Figure 2h) and reconnection electric field ~1.3 mV $m^{-1}$ for $B \approx 15$ nT and inflow ion speed of $\sim 0.1 V_{\mathrm{iA}} \approx 85$ km $s^{-1}$ (Figure 2b). We thus conclude that energy conversion at the X-point was ongoing. Note that the active X-point was captured inside the MMS tetrahedron during the ECS crossing (Figures 5a-d, 5g, and 5h), reinforcing the conclusions based on the reconstruction results.

In order to reveal how fast the magnetic island was growing, we calculated the amount of in-plane magnetic flux per unit length along **M** embedded between the reconstructed X- and O-points closer to the center of the reconstruction domain. Three cases are shown in Figure 6, one from the polynomial reconstruction and two from the EMHD reconstruction (see the caption of Figure 6 and Text S3 for details). Consistent with the island growth, the flux increases with time for all three cases (Figure 6a) and the measured component of the electric field along **M** ($E_M$) appears to vary in space and time (Figure 6c). However, the estimated rates of flux accumulation inside the island ($E_{\mathrm{Rec}}$ in Figure 6b) are about one order of magnitude smaller than the measured $E_M$ (flux injection rate) that is comparable to the expected reconnection electric field of ~1.3 mV $m^{-1}$. Tests of our reconstruction methods using simulated data show that the estimated fluxes may differ by a factor of 4 at most (Figure S3 and Texts S2 and S3). Thus, the result suggests that the in-plane magnetic field injected into the ECS was not ejected out of the X-point into the island, but annihilated around the X-point or O-point at the time and portion of the ECS observed by MMS. The small $E_{\mathrm{Rec}}$ inside the island (Figure 6) also indicates that the time evolution of the island was indeed slow, ensuring that the assumption of time-independence made in the EMHD reconstruction was approximately satisfied.

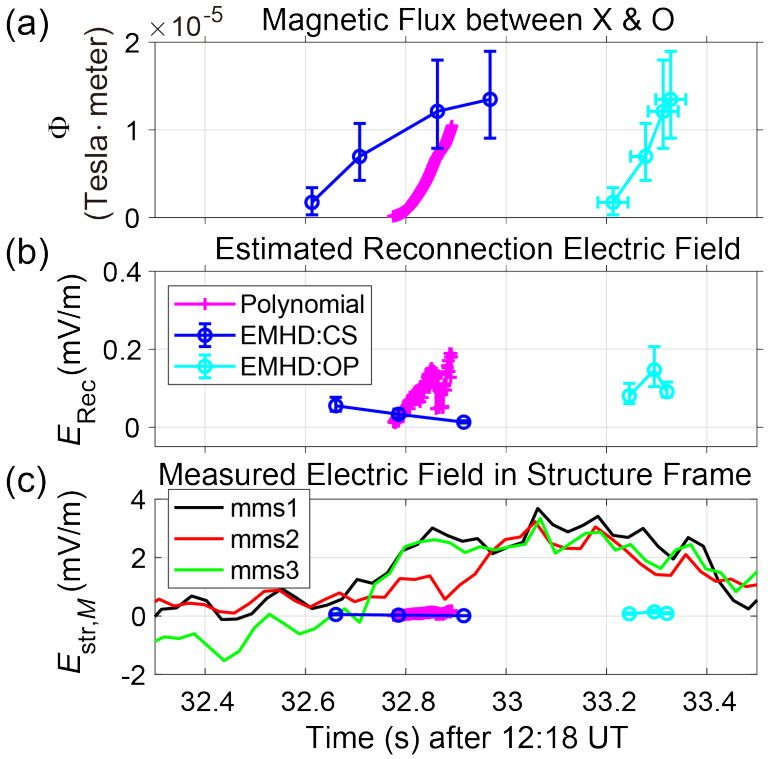


**Figure 6**. Reconnection electric fields, estimated from the EMHD and polynomial reconstructions, compared with the measured electric field. (a) In-plane magnetic flux ($\Phi$) embedded between the X- and O-points around the center of the reconstruction domain as a function of time. For the EMHD reconstruction, blue circules show the case when time is tagged by that of current sheet crossing ($B_L = 0$) by each spacecraft, while cyan circles show the case when time is tagged by that of closest approach to the reconstructed O-point. (b) Rate of flux accumulation inside the island ($E_{\rm Rec} = \frac{\partial \Phi}{\partial t}$). (c) $M$ component ($E_{str,M}$) of the electric field from MMS 1, MMS 2, and MMS 3 that made reliable electric field measurements, transformed into the frame comoving with the structure (see Text S3 for details), along with $E_{\rm Rec}$. The upper and lower levels of the error bars are based on results from the EMHD reconstructions with an offset of $B_z = +0.1$ nT or $-0.1$ nT in GSE added to the measurements, considering that the error in the magnetic field measurements is ~0.1 nT (Russell et al., 2016). The flux values from the polynomial reconstruction are shown only when both the X- and O-points are within twice the spacecraft separation of the centroid of the MMS spacecraft, based on results by Denton et al. (2021).

Since the reconstructed X-point may still be moving in the chosen structure frame, as suggested from Figures 5a-d, we estimate how much the electric field $\mathbf{E}_X$ in the frame of strictly stationary X-point may differ from $\mathbf{E}_{\rm str}$ (Figure 6c). Figures 5a-d suggest that the X-point moved $\lesssim 30$ km roughly in the $L$ direction

during the ~0.4 s interval of the ECS crossing by the four spacecraft (Figure 2e), indicating that the X-point speed in the structure frame was $\lesssim 100$ km $s^{-1}$. Since $|B_N| \lesssim 1$ nT for the reconstructed interval (Figure 2g), the estimated magnitude of the difference between $E_{str,M}$ and $E_{X,M}$ is $|\Delta E_M| \lesssim 0.1$ mV $m^{-1}$. This is much smaller than the measured $E_{str,M} \gtrsim 1.0$ mV $m^{-1}$, so that our conclusion that the flux accumulation rate inside the island (Figure 6b) was about one order of magnitude smaller than the flux injection rate is not affected.

## 4 Theoretical analysis

Is fast annihilation of the magnetic field as detected by MMS physically possible in an ECS? For quasi-steady 2-D reconnection in collisionless plasmas, electron demagnetization (violation of the electron frozen-in condition) at the X-line occurs when off-diagonal terms of the electron pressure tensor are significant (Hesse et al., 2011). Consistently, nongyrotropic electron velocity distributions as a manifestation of electron demagnetization have been observed in the present (Li et al., 2019) as well as other EDRs (Burch et al., 2016; Torbert et al., 2018). Earlier studies also demonstrated that the nongyrotropic electron pressure term can quantitatively account for the electric field ($E_M$) of fast reconnection as observed (Egedal et al., 2019). Here we demonstrate that magnetic-field annihilation may occur across $\mathbf{N}$ in an ECS extended in the $L$ direction with $\frac{\partial}{\partial M} = 0$, when the generalized Ohm's law is expressed by

$$\mathbf{E} = -\mathbf{v}_e \times \mathbf{B} + \frac{f(L,N)}{n_e e}\mathbf{M}. \quad (1)$$

Note that Eq. (1) has been used in the inertia-less version of the EMHD method (Sonnerup et al., 2016) with the following expression

$$f(L,N) = n_e\sqrt{2m_e k_B T_e}\frac{\partial v_{eL}}{\partial L}, \quad (2)$$

and Hesse et al. (2011) and Kuznetsova et al. (2007) have shown that Eq. (2) is applicable to the diffusion region of antiparallel reconnection.

We consider Faraday's law in the LMN coordinate system,

$$\frac{\partial \mathbf{B}}{\partial t} = -\nabla \times \mathbf{E} = \nabla \times (\mathbf{v}_e \times \mathbf{B}) - \frac{1}{n_e e}\nabla f(L,N) \times \mathbf{M}, \quad (3)$$

and discuss only the contribution of the second term on the right-hand side (RHS) of Eq. (3), because the first term does not violate the electron frozen-in condition. Furthermore, only the $L$ component

$$\frac{\partial B_L}{\partial t} \approx \frac{1}{n_e e}\frac{\partial f(L,N)}{\partial N} \quad (4)$$

is considered, because $B_N \approx 0$ in ECSs elongated in the $L$ direction. Since constant electron density, namely incompressible electron fluid ($\nabla \bullet \mathbf{v}_e = \frac{\partial v_{eL}}{\partial L} + \frac{\partial v_{eN}}{\partial N} = 0$), can be assumed in EDRs (Hesse et al., 2011; Sonnerup et al., 2016), the following relation results using Eq. (2)

$$\frac{\partial B_L}{\partial t} \approx -\frac{\sqrt{2m_e k_B T_e}}{e}\frac{\partial^2 v_{eN}}{\partial N^2}. \quad (5)$$

We note that a relation $-B_\infty v_{eN} \approx B_L V_\infty$ is approximately satisfied inside an EDR because the spatial variations along $\mathbf{N}$ of $B_L$ and $v_{eN}$ are very similar to each other with only sign difference (Figure 7), while in the inflow region outside of the EDR $|B_L v_{eN}| \approx E_0 = B_\infty V_\infty$ holds for quasi-steady 2-D reconnection (Liu et al., 2017). Here $E_0$ is the reconnection electric field, and $B_\infty$ and $V_\infty$ are the $B_L$ intensity and the electron inflow speed, respectively, immediately outside of the EDR, with $V_\infty \approx 0.1 V_{\mathrm{eA}}$ for fast reconnection where the electron Alfvén speed $V_{\mathrm{eA}} = \frac{B_\infty}{(\mu_0 m_e n_e)^{\frac{1}{2}}}$. Thus, the above relation becomes a diffusion equation for $B_L$

$$\frac{\partial B_L}{\partial t} \approx D_B \frac{\partial^2 B_L}{\partial N^2}, \quad (6)$$

where the diffusion coefficient $D_B = r_{\mathrm{ge}} V_\infty$ with gyroradius of thermal electrons $r_{\mathrm{ge}} = \frac{(2 m_e k_B T_e)^{\frac{1}{2}}}{(e B_\infty)}$. We can therefore conclude that in the presence of the term (2), equivalent to the nongyrotropic electron pressure tensor term, the in-plane magnetic-field component $B_L$ may be annihilated in an EDR, as long as the EDR thickness is of electron scale. This conclusion is consistent with the theoretical analysis (Hesse et al., 2011) in which the term (2) was derived by discussing a diffusion of the electron current density $j_{eM}$ that implies the annihilation of $B_L$. On the other hand, since the second term on the RHS of Eq. (3) has no $M$ component, no annihilation of $B_M$ (Hall magnetic field) occurs for 2-D reconnection. Moreover, the form of $D_B$ indicates that in principle fast magnetic-field annihilation may occur when fast inflow of the in-plane magnetic flux exists.

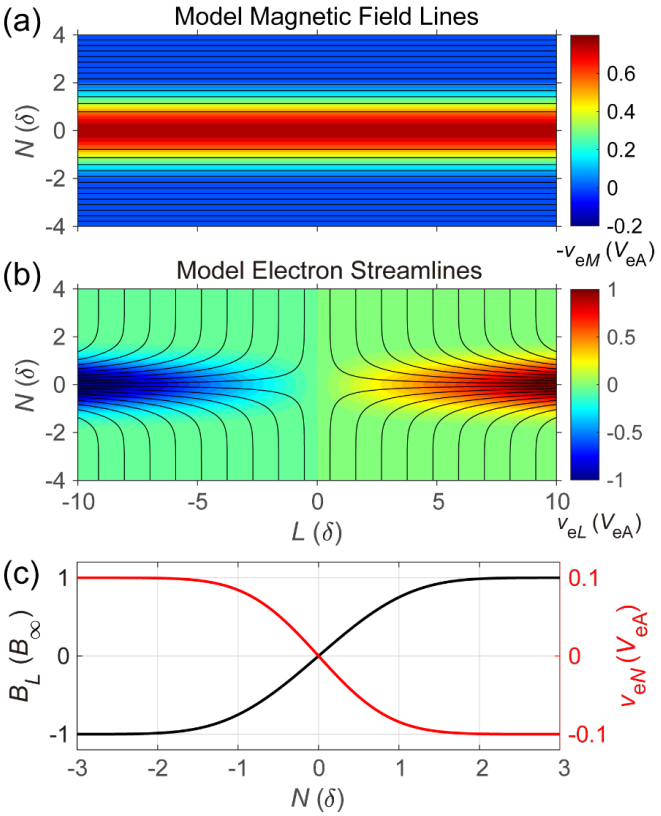


**Figure 7**. Exact solution of the dissipative EMHD equations (Sonnerup et al., 2016) showing the magnetic field and electron velocity profiles in and around an ECS with a thickness ($\delta$) comparable to $d_e$. (a) Magnetic field-lines in the $L$–$N$ plane with the out-of-plane ($-M$) component of the electron velocity in unit of $V_{\rm eA}$ in color. (b) Electron streamlines with the $L$ component ($v_{eL}$) of the electron velocity in color. (c) Spatial profiles along $\mathbf{N}$ of $v_{eN}$ and $B_L$ in unit of the field intensity ($B_\infty$) outside of the ECS.

The $B_L$ diffusion implied by Eq. (6) is consistent with an exact solution of the EMHD equations with the dissipation term (2) for a steady ECS, derived by Sonnerup et al. (2016), for which the inflowing $B_L$ is all annihilated rather than reconnected in the EDR (Figure 7). We can experimentally estimate the diffusion coefficient $D_{B,exp}$ assuming that the magnetic structure is quasi-steady so that the diffusion and convection terms are cancelled out, i.e., the RHS of Eq. (6) is equal to the $L$ component of the first term on the RHS of Eq. (3). For the observed ECS with a thickness $\delta \approx d_e$, the estimated coefficient $D_{B,exp} \approx \delta V_\infty = \frac{d_e E_{str,M}}{B_\infty} \sim 5 \times 10^9\ m^2 s^{-1}$, which is comparable to the theoretically predicted coefficient $D_B = r_{\rm ge} V_\infty \sim 10^{10}\ m^2 s^{-1}$ because the observed electron beta $\beta_e = \frac{{r_{\rm ge}}^2}{{d_e}^2} \sim 5$.

The fast collisionless annihilation is in stark contrast with annihilation in the classic (resistive magnetohydrodynamics) model (Parker, 1957; Sweet, 1958) of reconnection in an elongated current sheet that is negligible under magnetotail conditions. However, we do not exclude a likely possibility that at the sunward and anti-sunward ends of the present ECS, where the magnetic field may have had a Y-type geometry (Figure 8b,c), the magnetic field was efficiently reconnected and ejected downstream, as observed for other magnetotail reconnection events (Nakamura et al., 2018).

## 5 Summary and Discussion

The main results of our study can be summarized as follows. (1) The MMS observations reported in the present paper are consistent with fast energy conversion in an elongated EDR dominated by magnetic field annihilation (Figure 8); (2) the fully kinetic simulation shows annihilation-dominated energy conversion in and around electron-scale islands formed in the EDR elongated in the exhaust direction (Figure 1); and (3) theoretical analysis suggests that fast collisionless magnetic diffusion can occur in a planar EDR with nongyrotropic electrons (section 4). Thus, three different approaches, namely, our MMS event analysis, simulation, and theoretical analysis all support magnetic field annihilation in an elongated EDR. The discovery of the annihilation in a reconnecting ECS could have far-reaching implications for how magnetic energy is dissipated in plasma turbulence in the collisionless regime, because reconnection has been suggested to play a role in the dissipation process (Matthaeus and Lamkin, 1986; Retinò et al., 2007; Servidio et al., 2009).

The collisionless annihilation on the electron scale may not be surprising, but we note that no earlier study has shown that its signatures are identifiable. This is probably because observable signatures are nearly the same as of standard reconnection if an observing probe is located in regions outside of the EDR or downstream of the Y-points (Figure 8b,c).

An important question remains about whether the magnetic energy dissipated by the annihilation is partitioned to thermal or nonthermal electrons, if not to the electron bulk flow. Recently, Nakamura et al. (2021) have shown, based on a fully kinetic simulation, that electrons are strongly heated in electron-scale magnetic islands where the annihilation is ongoing. In the present event, however, no clear signature of electron heating or energization was identified, likely because electron beta $\beta_e$ outside the EDR was so high (~5) that available magnetic energy was probably too small for energization effects to be identified; even if all the magnetic energy was converted to electron thermal energy, the temperature increase would be only about 20% of the ambient value. It is noted that for typical reconnection, only ~2% of the available magnetic energy is partitioned to thermal electrons in reconnection exhausts (Phan et al., 2013). Thus, the process of energy partition through the annihilation will need to be quantitatively assessed in the future.

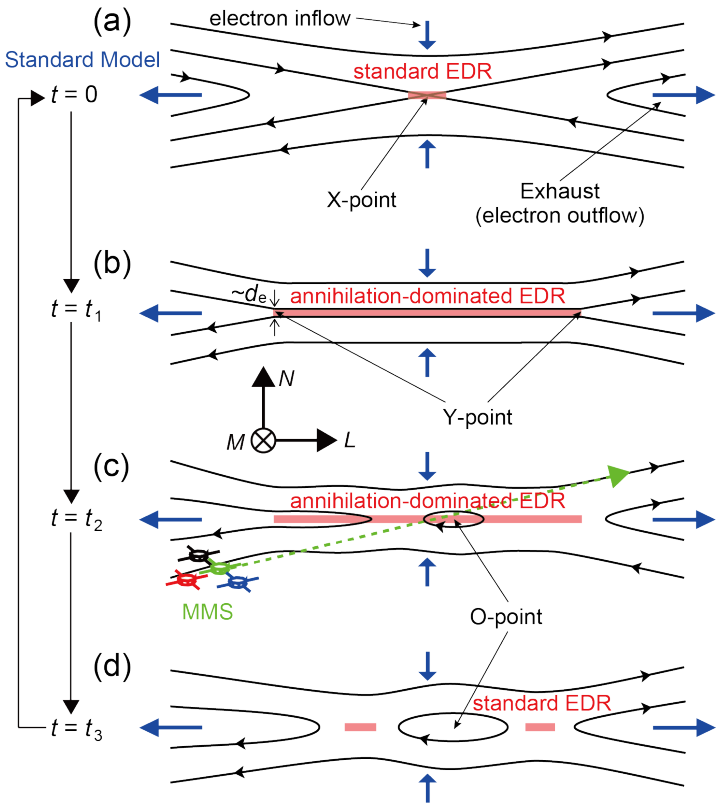


**Figure 8**. Possible sequence of time evolution of the electron-scale current sheet observed by MMS on 10 August 2017. (a) Standard EDR with an X-type magnetic field geometry where the magnetic-to-particle energy conversion is mostly due to magnetic topology change (Torbert et al., 2018). (b) EDR after elongation along $L$, as seen in kinetic simulations (Daughton et al., 2006; Figure 1), where the energy conversion may be mostly due to magnetic field annihilation (section 4; see also Nakamura et al., 2021). (c) Initial stage of the magnetic island formation in the EDR, as observed by MMS. (d) Possible later stage of the island growth in exhausts of the EDRs, as seen in simulations (Figure 1).

One may raise the possibility that the elongation of the EDR is rare or the length of the elongated EDR is only a few times that of standard EDR at most, so that the annihilation would not have any significant impact. This may be the case in situations where reconnection occurs spontaneously. However, ECSs can be generated frequently or at many locations in turbulent plasma or through flow shear instabilities (Nakamura et al., 2013), and an integrated effect of the annihilation in such ECSs may not be negligible. On the other hand, the elongated EDR is unstable to the formation of electron-scale magnetic islands (Nakamura et al., 2021), so that the annihilation may only be a transient process, in contrast to

the steady-state solution as shown in Figure 7. Both the simulation (Figure 1) and observations (section 3.5) suggest that the annihilation may last for about one ion cyclotron period for each cycle of electron-scale island formation.

While the present observations and theory have shown that magnetic field annihilation can occur in a high $\beta_e$ ECS across which the magnetic fields are nearly antiparallel, it remains unknown whether the annihilation can occur under low $\beta_e$ and significant guide field conditions when electrons are magnetized more strongly. This is because the dissipation term (2) may not be applicable to guide field cases and the diffusion coefficient $D_B = r_{\rm ge} V_\infty$ in Eq. (6) becomes small under low $\beta_e$ or small $r_{\rm ge}$ conditions. Since guide-field reconnection is quite common in the solar wind (Vasko et al., 2021) and magnetosheath (Phan et al., 2018), and reconnection in the solar corona or inner heliosphere can occur under low beta conditions, it would be worthwhile to explore the properties of the collisionless annihilation under more general conditions.

Acknowledgments, and Data

All MMS data used in this study are publicly available via the MMS Science Data Center at https://lasp.colorado.edu/mms/sdc/public/. All code used to analyze the MMS data in this study is based on the publicly available SPEDAS tools (Angelopoulos et al., 2019) (http://spedas.org/blog/), except for the Matlab code for the EMHD and polynomial reconstructions. The Matlab code for the EMHD reconstruction can be found at the Zenodo (https://doi.org/10.5281/zenodo.3900642), and that for the polynomial reconstruction at https://doi.org/10.5281/zenodo.3906853. H.H. thanks W. Daughton for discussions. We are grateful for the dedicated efforts of the MMS team. For the simulation reported in this paper, we acknowledge PRACE for awarding us access to MareNostrum at the Barcelona Supercomputing Center (BSC), Spain. The work by H.H. was supported by JSPS Grant-in-aid for Scientific Research KAKENHI 21K03504. R.E.D was supported by a NASA grant (80NSSC19K0254). T.K.M.N. was supported by the Austrian Research Fund (FWF) P32175-N27.

References

Angelopoulos, V., McFadden, J. P., Larson, D., et al. (2008). Tail reconnection triggering substorm onset. *Science*, *321*, 931–935.

Angelopoulos, V., Cruce, P., Drozdov, A., et al. (2019). The Space Physics Environment Data Analysis System (SPEDAS). *Space Sci. Rev.*, *215*, 9. https://doi.org/10.1007/s11214-018-0576-4.

Burch, J. L., Torbert, R. B., Phan, T. D., et al. (2016). Electron-scale measurements of magnetic reconnection in space. *Science*, *352*, aaf2939. doi:10.1126/science.aaf2939.

Daughton, W., Scudder, J., & Karimabadi, H. (2006). Fully kinetic simulations of undriven magnetic reconnection with open boundary conditions. *Phys. Plasmas*, *13*, 072101. https://doi.org/10.1063/1.2218817.

Denton, R. E., Sonnerup, B. U. Ö., Hasegawa, H., et al. (2016). Motion of the MMS spacecraft relative to the magnetic reconnection structure observed on 16 Oct 2015 at 1307 UT. *Geophys. Res. Lett.*, *43*, 5589–5596. doi:10.1002/2016GL069214.

Denton, R. E., Sonnerup, B. U. Ö., Russell, C. T., et al. (2018). Determining L-M-N current sheet coordinates at the magnetopause from Magnetospheric Multiscale data. *J. Geophys. Res. Space Physics*, *123*, 2274–2295. https://doi.org/10.1002/2017JA024619.

Denton, R. E., Torbert, R. B., Hasegawa, H., et al. (2020). Polynomial reconstruction of the reconnection magnetic field observed by multiple spacecraft. *J. Geophys. Res. Space Physics*, *125*, e2019JA027481. https://doi.org/10.1029/2019JA027481.

Denton, R. E., Torbert, R. B., Hasegawa, H., et al. (2021). Two-dimensional velocity of the magnetic structure observed on 11 July 2017 by the Magnetospheric Multiscale spacecraft, *J. Geophys. Res. Space Physics*, *126*, e2020JA028705, https://doi.org/10.1029/2020JA028705.

Dunlop, M. W., Balogh, A., Glassmeier, K.-H., & Robert, P. (2002). Four-point Cluster application of magnetic field analysis tools: The Curlometer. *J. Geophys. Res.*, *107*, 1384. doi:10.1029/2001JA005088.

Egedal, J., Ng, J., Le, A., et al. (2019). Pressure tensor elements breaking the frozen-in law during reconnection in Earth's magnetotail. *Phys. Rev. Lett.*, *123*, 225101. doi:10.1103/PhysRevLett.123.225101.

Ergun, R. E., Tucker, S., Westfall, J., et al. (2016). The axial double probe and fields signal processing for the MMS mission. *Space Sci. Rev.*, *199*, 167–188. doi:10.1007/s11214-014-0115-x.

Fujimoto, K. (2006). Time evolution of the electron diffusion region and the reconnection rate in fully kinetic and large system. *Phys. Plasmas*, *13*, 072904.

Hasegawa, H., Sonnerup, B. U. Ö., Denton, R. E., et al. (2017). Reconstruction of the electron diffusion region observed by the Magnetospheric Multiscale spacecraft: First results. *Geophys. Res. Lett.*, *44*, 4566–4574. doi:10.1002/2017GL073163.

Hasegawa, H., Denton, R. E., Nakamura, R., et al. (2019). Reconstruction of the electron diffusion region of magnetotail reconnection seen by the MMS spacecraft on 11 July 2017. *J. Geophys. Res. Space Physics*, *124*, 122–138. https://doi.org/10.1029/2018JA026051.

Hasegawa, H., Nakamura, T. K. M., & Denton, R. E. (2021). Reconstruction of the electron diffusion region with inertia and compressibility effects. *Journal of Geophysical Research: Space Physics*, *126*, e2021JA029841. https://doi.org/10.1029/2021JA029841.

Hesse, M., Neukirch, T., Schindler, K., Kuznetsova, M., & Zenitani, S. (2011).

The diffusion region in collisionless magnetic reconnection. *Space Sci. Rev.*, *160*, 3–23. doi:10.1007/s11214-010-9740-1.

Jain, N., & Sharma, A. S. (2015). Evolution of electron current sheets in collisionless magnetic reconnection, *Phys. Plasmas*, *22*, 102110, doi:10.1063/1.4933120.

Kawano, H., & Higuchi, T. (1995). The bootstrap method in space physics: Error estimation for minimum variance analysis. *Geophys. Res. Lett.*, *22*, 307–310. doi:10.1029/94GL02969.

Kuznetsova, M. M., Hesse, M., Rastaetter, L., et al. (2007). Multiscale modeling of magnetospheric reconnection, *J. Geophys. Res.*, *112*, A10210. doi:10.1029/2007JA012316.

Li, X., Wang, R., Lu, Q., et al. (2019). Observation of nongyrotropic electron distribution across the electron diffusion region in the magnetotail reconnection. *Geophys. Res. Lett.*, *46*, 14263–14273. https://doi.org/10.1029/2019GL085014.

Lindqvist, P.-A., Olsson, G., Torbert, R. B., et al. (2016). The Spin-plane Double Probe electric field instrument for MMS. *Space Sci. Rev.*, *199*, 137–165. doi:10.1007/s11214-014-0116-9.

Liu, Y.-H., Hesse, M., Guo, F., et al. (2017). Why does steady-state magnetic reconnection have a maximum local rate of order 0.1? *Phys. Rev. Lett.*, *118*, 085101. doi:10.1103/PhysRevLett.118.085101.

Matthaeus, W. H., & Lamkin, S. L. (1986). Turbulent magnetic reconnection. *Phys. Plasmas*, *29*(8), 2513–2534. https://doi.org/10.1063/1.866004.

Nagai, T., Shinohara, I., Fujimoto, M., et al. (2001). Geotail observations of the Hall current system: Evidence of magnetic reconnection in the magnetotail. *J. Geophys. Res.*, *106*, 25929–25949.

Nagai, T., Shinohara, I., Fujimoto, M., Matsuoka, A., Saito, Y., & Mukai, T. (2011). Construction of magnetic reconnection in the near-Earth magnetotail with Geotail. *J. Geophys. Res.*, *116*, A04222. doi:10.1029/2010JA016283.

Nakamura, T. K. M., Daughton, W., Karimabadi, H., & Eriksson, S. (2013). Three-dimensional dynamics of vortex-induced reconnection and comparison with THEMIS observations, *J. Geophys. Res. Space Physics*, *118*, 5742-5757, doi:10.1002/jgra.50547.

Nakamura, T. K. M., Genestreti, K. J., Liu, Y.-H., et al. (2018). Measurement of the magnetic reconnection rate in the Earth's magnetotail. *J Geophys. Res. Space Physics*, *123*, 9150–9168. https://doi.org/10.1029/2018JA025713.

Nakamura, T. K. M., Stawarz, J. E., Hasegawa, H., Narita, Y., Franci, L., Wilder, F. D. et al. (2020). Effects of fluctuating magnetic field on the growth of the Kelvin-Helmholtz instability at the Earth's magnetopause. *Journal of Geophysical Research: Space Physics*, *125*, e2019JA027515. https://doi.org/10.1029/2019JA027515.

Nakamura, T. K. M., Hasegawa, H., Genestreti, K. J., Denton, R. E., Phan, T. D., Stawarz, J. E., et al. (2021). Fast cross-scale energy transfer during turbulent magnetic reconnection. *Geophysical Research Letters*, *48*, e2021GL093524. https://doi.org/10.1029/2021GL093524.

Øieroset, M., Phan, T. D., Fujimoto, M., Lin, R. P., & Lepping, R. P. (2001). In situ detection of collisionless reconnection in the Earth's magnetotail. *Nature*, *412*, 414–417.

Parker, E. N. (1957). Sweet's mechanism for merging magnetic fields in conducting fluids. *J. Geophys. Res.*, *62*, 509–520.

Phan, T. D., Shay, M. A., Gosling, J. T., et al. (2013). Electron bulk heating in magnetic reconnection at Earth's magnetopause: Dependence on the inflow Alfven speed and magnetic shear. *Geophys. Res. Lett.*, *40*, 4475–4480. doi:10.1002/grl.50917.

Phan, T. D., Eastwood, J. P., Shay, M. A., Drake, J. F., Sonnerup, B. U. Ö., et al. (2018). Electron magnetic reconnection without ion coupling in Earth's turbulent magnetosheath, *Nature*, *557*, 202-206, doi:10.1038/s41586-018-0091-5.

Pollock, C., Moore, T., Jacques, A., et al. (2016). Fast plasma investigation for Magnetospheric Multiscale. *Space Sci. Rev.*, *199*, 331–406. doi:10.1007/s11214-016-0245-4.

Retinò, A., Sundkvist, D., Vaivads, A., Mozer, F., André, M., & Owen, C. J. (2007). In situ evidence of magnetic reconnection in turbulent plasma. *Nature Physics*, *3*, 235–238. doi:10.1038/nphys574.

Rezeau, L., Belmont, G., Manuzzo, R., Aunai, N., & Dargent, J. (2018). Analyzing the magnetopause internal structure: New possibilities offered by MMS tested in a case study. *J. Geophys. Res. Space Physics*, *123*, 227–241. https://doi.org/10.1002/2017JA024526.

Russell, C. T., Anderson, B. J., Baumjohann, W., et al. (2016). The Magnetospheric Multiscale Magnetometers, *Space Sci. Rev.*, *199*, 189–256. doi:10.1007/s11214-014-0057-3.

Servidio, S., Matthaeus, W. H., Shay, M. A., Cassak, P. A., & Dmitruk, P. (2009). Magnetic reconnection in two-dimensional magnetohydrodynamic turbulence. *Phys. Rev. Lett.*, *102*, 115003.

Shay, M. A., Drake, J. F., & Swisdak, M. (2007). Two-scale structure of the electron dissipation region during collisionless magnetic reconnection. *Phys. Rev. Lett.*, *99*, 155002. doi:10.1103/PhysRevLett.99.155002.

Shi, Q. Q., Tian, A. M., Bai, S. C., et al. (2019). Dimensionality, coordinate system and reference frame for analysis of in-situ space plasma and field data. *Space Sci. Rev.*, *215*, 35. https://doi.org/10.1007/s11214-019-0601-2.

Sonnerup, B. U. Ö., & Scheible, M. (1998). Minimum and maximum variance analysis, in *Analysis Methods for Multi-Spacecraft Data*, G. Paschmann, P. W.

Daly, Eds., ISSI/ESA, chap. 8, pp. 185–220.

Sonnerup, B. U. Ö., Hasegawa, H., Denton, R. E., & Nakamura, T. K. M. (2016). Reconstruction of the electron diffusion region. *J. Geophys. Res. Space Physics*, *121*, 4279–4290. doi:10.1002/2016JA022430.

Sweet, P. A. (1958). The neutral point theory of solar flares, in *Electromagnetic Phenomena in Cosmical Physics*, B. Lehnert, Ed., Cambridge, pp. 123–134.

Torbert, R. B., Russell, C. T., Magnes, W., et al. (2016). The FIELDS instrument suite on MMS: scientific objectives, measurements, and data products. *Space Sci. Rev.*, *199*, 105–135. doi:10.1007/s11214-014-0109-8.

Torbert, R. B., Burch, J. L., Phan, T. D., et al. (2018). Electron-scale dynamics of the diffusion region during symmetric magnetic reconnection in space. *Science*, *362*, 1391–1395. doi:10.1126/science.aat2998.

Torbert, R. B., Dors, I., Argall, M. R., et al. (2020). A new method of 3-D magnetic field reconstruction. *Geophys. Res. Lett.*, *47*, e2019GL085542. https://doi.org/10.1029/2019GL085542.

Vasko, I. Y., Alimov, K., Phan, T. D., Bale, S. D., Mozer, F. S., & Artemyev, A. V. (2021). Kinetic-scale current sheets in the solar wind at 1 au: Properties and the necessary condition for reconnection, *Astrophys. J. Lett.*, *923*, L19, https://doi.org/10.3847/2041-8213/ac3f30.

Zenitani, S., Hesse, M., Klimas, A., & Kuznetsova, M. (2011). New measure of the dissipation region in collisionless magnetic reconnection. *Phys. Rev. Lett., 106*, 195003. doi:10.1063/1.3554655.

Zhou, M., Deng, X. H., Z. H. Zhong, et al. (2019). Observations of an electron diffusion region in symmetric reconnection with weak guide field. *Astrophys. J.*, *870*, 34. https://doi.org/10.3847/1538-4357/aaf16f.